2698–2708 *Nucleic Acids Research, 2013, Vol. 41, No. 4* *Published online 28 December 2012*
doi:10.1093/nar/gks1322

Thermodynamic properties distinguish human mitochondrial aspartyl-tRNA synthetase from bacterial homolog with same 3D architecture

Anne Neuenfeldt, Bernard Lorber, Eric Ennifar, Agnès Gaudry, Claude Sauter, Marie Sissler and Catherine Florentz*

Architecture et Réactivité de l'ARN, Université de Strasbourg, CNRS, IBMC, F-67084 Strasbourg Cedex, France

Received August 31, 2012; Revised November 17, 2012; Accepted November 22, 2012

ABSTRACT

In the mammalian mitochondrial translation apparatus, the proteins and their partner RNAs are coded by two genomes. The proteins are nuclear-encoded and resemble their homologs, whereas the RNAs coming from the rapidly evolving mitochondrial genome have lost critical structural information. This raises the question of molecular adaptation of these proteins to their peculiar partner RNAs. The crystal structure of the homodimeric bacterial-type human mitochondrial aspartyl-tRNA synthetase (DRS) confirmed a 3D architecture close to that of *Escherichia coli* DRS. However, the mitochondrial enzyme distinguishes by an enlarged catalytic groove, a more electropositive surface potential and an alternate interaction network at the subunits interface. It also presented a thermal stability reduced by as much as 12°C. Isothermal titration calorimetry analyses revealed that the affinity of the mitochondrial enzyme for cognate and non-cognate tRNAs is one order of magnitude higher, but with different enthalpy and entropy contributions. They further indicated that both enzymes bind an adenylate analog by a cooperative allosteric mechanism with different thermodynamic contributions. The larger flexibility of the mitochondrial synthetase with respect to the bacterial enzyme, in combination with a preserved architecture, may represent an evolutionary process, allowing nuclear-encoded proteins to cooperate with degenerated organelle RNAs.

INTRODUCTION

Mitochondria are of endosymbiotic origin and have undergone massive gene transfer to the host nucleus during evolution (1). On sharp reduction (~70-fold) to a 16.6 kb circular mammalian mitochondrial (mt) DNA, only 37 genes remain coding for 13 respiratory chain subunits, 22 tRNAs and 2 rRNAs (2). The faster evolutionary rate of mt-DNA than the nuclear genome (3,4) leads to abnormal RNAs, shrunken in size and often lacking important signals. mRNAs are deprived of 3′- and 5′-untranslated regions, rRNAs are smaller than their bacterial or eukaryotic homologs, and an RNA moiety for RNase P is absent (5–7). Most mt-tRNAs have shortened sequences, miss crucial folding and recognition nucleotides as compared with 'classical' tRNAs and are more flexible (6,8–10). Hence, preservation of mitochondrial translation relies on a continued adaptation of proteins to the peculiarities of partner RNAs. One compensatory mechanism consists in an increase in the number and/or size of partner proteins (encoded in the nucleus and imported) that take over the role of missing RNA domains. For instance, bovine mt-ribosomes contain 30 proteins in the small subunits and 48 in the large subunits, instead of 21 and 33, respectively, in prokaryotes, with N- or C-terminal extensions (11,12). Human RNase P is fully proteinaceous with three protein subunits (7).

Mechanisms to compensate for degeneration of mammalian mt-tRNAs remain mainly unsolved, especially for mt aminoacyl-tRNA synthetases (mt-aaRSs; specificity indicated by the amino acid abbreviated in a one-letter code, the origin of the aaRS is indicated by a three-letter abbreviation of the organism's name with the

*To whom correspondence should be addressed. Tel: +33 3 88 41 70 59; Fax: +33 3 88 60 22 18; Email: C.Florentz@unistra.fr
Present address:
Anne Neuenfeldt, Cyano Biofuels GmbH, Magnusstr. 11, D-12489 Berlin, Germany.

mitochondrial origin given by the digit 2 e.g. *Hsa*DRS2 for *Homo sapiens* mitochondrial aspartyl-tRNA synthetase), the enzymes which activate and bind a specific amino acid to their cognate tRNA (13). These enzymes are nuclear encoded and, with only few exceptions, are of about the same size, have the same structural 2D organization and contain the expected specificity signals and synthetase class signatures as bacterial and cytosolic aaRSs (14–17). The first 3D structures of mammalian mt-aaRSs confirmed the absence of additional domains (18–21).

Properties of mammalian mt-aaRSs enabling them to deal with mt-tRNAs remain mainly unknown (9,22,23). On one side, their catalytic efficiency is usually one to two orders of magnitude below that of bacterial aaRSs, aminoacylation identity rules rely either on minimalist sets of determinants in the tRNA or even are disobeyed (22,23). On the other hand, a long standing remarkable feature of mt-aaRSs is their high capacity in tRNA accommodation: mt-aaRSs charge both mt- and bacterial tRNAs, whereas bacterial aaRSs cannot cross-aminoacylate mt-tRNAs (24). Non-aminoacylation of an mt-tRNA by a bacterial enzyme is linked to the absence of essential identity signals and to the large flexibility of the mt-tRNA (25). These data suggest the existence of peculiar dynamic properties for the mt-aaRSs, which are not shared with a bacterial homolog.

Here, we compared several biophysical properties of human mitochondrial aspartyl-tRNA synthetase, *Hsa*DRS2, with them to those of a bacterial (*E. coli)* homolog, *Eco*DRS. The crystal structure of *Hsa*DRS2 was solved, thermal stabilities were quantified, and thermodynamic parameters of substrate binding were determined by isothermal titration calorimetry. As an outcome, both proteins share a common 3D architecture but the mammalian mt-aaRS gained in plasticity, enabling it to handle any $tRNA^{Asp}$ and especially the non-canonical mt-$tRNA^{Asp}$. We propose that enlarged plasticity represents a co-evolution mechanism of the nuclear and mt genomes in eukaryotic cells subjected to highly different evolutionary pressures. This plasticity will be an important parameter to consider for the molecular understanding of a rapidly increasing number of human disorders linked to mutations in mt-aaRSs.

MATERIALS AND METHODS

Protein and tRNA purification

*Eco*DRS was overproduced in *E. coli* JM83, purified to homogeneity and concentrated to 40 mg ml^{-1} (25). *Hsa*DRS2 [mt-AspRS(I41) in (26); Supplementary Figure S1] was cloned into pDEST14 using the Gateway technology (Invitrogen) and overproduced in *E. coli* BL21 (DE3) Rosetta 2 strain as described (26). It was purified by affinity chromatography on an Ni-NTA column followed by gel filtration and concentrated to 20 mg ml^{-1} (concentration of monomers) in 50 mM of HEPES–Na pH 7.5, 150 mM of NaCl, 1 mM of DTT, 0.1 mM of ethylenediaminetetraacetic acid and 10% (v/v) of glycerol. This buffer, called herein 'isothermal titration calorimetry (ITC) buffer', prevents denaturation of the mt-aaRS for several days as verified by dynamic light scattering (DLS) (Supplementary Figure S2). Magnesium had to be kept out, as even low concentrations led to precipitation of HsaDRS2. It was also used for the preparation of *Eco*DRS and of the tRNAs. tRNAs (sequences are indicated in Supplementary Figure S1) were produced by *in vitro* transcription and were purified to single nucleotide resolution on denaturing 12% polyacrylamide gel electrophoresis. They were solubilized in ITC buffer and denatured/renatured before use as described (16).

Aminoacylation

Assays were performed at 25°C on transcripts as described previously (16,27). Specific activities were measured by incubating 0.2–3 nM *Eco*DRS or 77–930 nM *Hsa*DRS2, with an excess of 4 μM cognate or non-cognate transcript. Kinetic parameters k_{cat} and K_M were derived from assays containing 2 nM of *Eco*DRS or 50 nM of *Hsa*DRS2 with 0.2–4 μM of *Eco* $tRNA^{Asp}$ or mt-$tRNA^{Asp}$ transcript.

Crystallography

Crystallization conditions were searched at 20°C using commercial kits as described (26). *Hsa*DRS2 was crystallized by vapor diffusion with 10% (m/v) PEG-3350 and 0.5 M of ammonium sulfate as crystallants in 25 mM of Bis–Tris pH 5.5 (26). Resulting needle-like crystals ($\sim 300 \times 20 \times 20\,\mu m^3$) were cryocooled in their mother liquor. They were extremely radiation sensitive and diffracted weakly. Complete data sets were collected with a fast PILATUS 6 M pixel detector (DECTRIS) at the X06DA beamline, Swiss Light Source (Villigen). Diffraction data at 3.7Å resolution in P2 space group were processed using XDS and XSCALE (28) and were converted into structure factors without any sigma cut-off using *TRUNCATE* from the CCP4 package (29). Molecular replacement solutions were sought with data truncated at 4.5 Å using a homology model derived from the structure of *Eco*DRS (30) and the PHASER program (31) as implemented in the PHENIX package (32). Two *Hsa*DRS2 dimers were identified in the monoclinic asymmetric unit. Refinement using a dynamic elastic network (DEN) as implemented in CNS 1.3 (33) led to a reorientation of the insertions and to a dramatic improvement of the electron density map. All residues of *Hsa*DRS2 were built except the 26 C-terminal amino acids (including the 6-His tag), which are disordered. The final coordinates (residues 42–630 for each of the four monomers) and the experimental data have been deposited with the PDB (ID: 4AH6). Figures were prepared with Pymol (www.pymol.org), electrostatic surface potentials were calculated using its APBS plug-in and are depicted at the same color scale in all figures.

Dynamic light scattering

Particle size analysis was performed at 25°C using a Malvern Zetasizer NanoS instrument and a 40 μl quartz cell containing 20 μl of protein solution at 0.5–8 mg ml^{-1} in ITC buffer. Five consecutive measurements were collected in automatic mode, and data were processed with

the manufacturer's software. The hydrodynamic diameter d_h was derived from diffusion coefficient via the Stokes–Einstein relation and was corrected for solvent viscosity and refractive index. Thermal stability was estimated by subjecting protein at 3 mg ml^{-1} to temperature gradients from 20°C to 80°C. The temperature at which particle size was increased by a factor 2 was taken as the melting point Tm. Additives were prepared in water.

Differential scanning fluorimetry

Samples made of 20 µl protein solution at 3 mg ml^{-1} and 0.5 µl of SYPRO Orange™ 5000 × stock diluted 20-fold in dimethlsulfoxyde (DMSO) were transferred in 0.2 ml tubes. Additives prepared as described earlier in the text were brought in 1 µl samples, so that their final concentration was as indicated. The variation of fluorescence intensity during a temperature gradient from 25°C to 95°C was monitored in a Stratagene Mx3005P quantitative polymerase chain reaction instrument. On unfolding of the protein, hydrophobic residues become accessible to the dye, which becomes fluorescent (34). Melting point Tm was deduced from maximum of the derivative plot. They are ~5°C higher as compared with data obtained by the DLS method.

Synchrotron radiation circular dichroism

The experimental set-up at the DISCO beamline, SOLEIL synchrotron (Saint-Aubin, France) was calibrated for magnitude and polarization with a 6.1 mg/ml D-10-camphorsulfonic acid solution. Ten micrograms per milliliter of DRS solutions in 100 mM of potassium phosphate, 50 mM of KCl, 10% (v/v) of glycerol and 1 mM of Tris(2-carboxyethyl)phosphine hydrochloride, TCEP, were placed in a CaF_2 cuvette, with an optical path of 8 µm. Three spectra between 170 and 280 nm were recorded at temperatures ranging from 20°C to 80°C by 4°C steps to assess the thermal stability of *Eco*DRS and *Hsa*DRS2. Data were processed (spectrum averaging and solvent baseline subtraction) using CDtool (35).

Isothermal titration calorimetry

Before ITC measurements, conditions were determined in which the four investigated macromolecules (*Hsa*DRS2, *Eco*DRS, *Hsa* mt-$tRNA^{Asp}$ and *Eco* $tRNA^{Asp}$) were stable during the time of the experiment. This was found to be the case in the so-called 'ITC buffer' (50 mM of HEPES–Na pH 7.5, 150 mM of NaCl, 1 mM of DTT, 0.1 mM of ethylenediaminetetraacetic acid and 10% of glycerol). Magnesium had to be omitted, as it leads to precipitation of *Hsa*DRS. To eliminate possible errors to ITC experiments, all samples (proteins and tRNAs) were extensively and extemporaneously dialyzed against a same stock solution of 'ITC buffer', degassed with argon and ultracentrifuged at 4°C. ITC experiments were performed at 25°C in a MicroCal iTC_{200} instrument (GE Healthcare). In a typical experiment, 2 µl samples of 300 µM *Eco*DRS or of 100 µM *Hsa*DRS2 were injected into 200 µl of 36 µM or 11 µM, respectively, cognate tRNA transcript solution. Injections lasted 4 s at 120 s intervals. Cross-bindings were also performed with protein/RNA concentration in a ~10:1 molar ratio. Retrieved ΔH and ΔG values were used to calculate the binding entropy ΔS (expressed as $-T\Delta S$, with $\Delta G = \Delta H - T\Delta S$). The adenylate analog 5′-*O*-[*N*-(L-aspartyl)sulfamoyl] adenosine (Asp–AMS) was titrated against 200 µl of enzyme with 0.7 µl injections to *Hsa*DRS2 at 32 µM and 1.5 µl to *Eco*DRS at 45 µM. Data were analyzed with the Origin software.

RESULTS

Solution properties of *Hsa*DRS2

*Hsa*DRS2 and *Eco*DRS are homologous dimeric enzymes, both of bacterial evolutionary type, sharing a same size and 43% sequence identity, including all typical signature motifs of DRSs and the same secondary structure organization (16,36) (Supplementary Figure S1). Recombinant proteins were overexpressed in *E. coli* and the final enzymatic preparations brought into the same buffer ('ITC buffer', see 'Materials and Methods' section) suitable for ultimate comparative isothermal titration calorimetry experiments. These conditions were a compromise for non-aggregation of *Hsa*DRS2, the more sensitive of the two enzymes (27), preservation of activity for both enzymes and stability of the tRNAs. *Hsa*DRS2 studied herein is deprived of the 40 first amino acids likely encompassing the mitochondrial targeting sequence (26). Both proteins had the same mean hydrodynamic diameter (d_h) of 10 ± 1 nm in DLS, in agreement with a homodimeric structure (Supplementary Figure S2). Kinetic parameters and catalytic efficiencies of both enzymes tested under identical conditions confirmed the ~60-fold higher aminoacylation rate and efficiency in the *Eco*DRS cognate system compared with *Hsa*DRS2 (Table 1). However, *Eco*DRS was unable to aminoacylate the mt-tRNA, whereas the mt-aaRS charged both cognate and non-cognate tRNAs with similar efficiency.

Crystal structure of *Hsa*DRS2

Single needle-like crystals of *Hsa*DRS2 were obtained in the presence of PEG-3550 and ammonium sulfate (26). They yielded a complete diffraction data set (26). In spite of their modest resolution (3.7 Å), these data were suitable to determine the architecture of *Hsa*DRS2 (26). The structure, solved herein by molecular replacement using a homology model derived from the structure of the *Eco*DRS (30), confirmed the dimeric status of the enzyme. It clearly showed the anticodon binding and catalytic domains of the monomers but did not enable visualization of the bacterial insertion domain (residues 337–470, Supplementary Figure S1). This suggested either a structural rearrangement or a local flexibility of this domain. The ambiguity was solved by using a DEN-assisted refinement procedure (33) that allowed repositioning of the insertion in well-defined electron density (Supplementary Figure S3 and Table 2). This domain reorientation, different from *Eco*DRS, was not an effect of crystal packing because the four independent monomers in the asymetric unit adopted the same conformation.

Table 1. Comparative kinetic properties of *Hsa*DRS2 and *Eco*DRS in tRNA aspartylation

DRS[a]	$tRNA^{Asp}$ (transcript)	k_{cat} (10^{-3} sec^{-1})	K_M (μM)	k_{cat}/K_M (10^{-3} sec^{-1} μM^{-1})	L	$\Delta\Delta G^b$ (kcal mol^{-1})
*Hsa*DRS2	mt	4.0 ± 0.4	1.1 ± 0.2	3.7 ± 0.7	72	−2.45
*Hsa*DRS2	*Eco*	10.3 ± 2.0	1.2 ± 0.1	8.3 ± 0.8	35	−2.04
*Eco*DRS	*Eco*	230 ± 6.0	0.8 ± 0.1	293 ± 14.4	1	–
*Eco*DRS	mt	nd	nd	nd	$>10^6$	

All data were obtained at 25°C (T = 298°K) and correspond to mean values from at least duplicated experiments with independent and freshly prepared enzyme and tRNA lots.
[a]k_{cat} and K_M values were derived from assays containing 2 nM of *Eco*DRS or 50 nM of *Hsa*DRS2 and 0.2–4 μM of *Eco* or *Hsa* mt-tRNA transcript. L stands for the relative loss in aminoacylation efficiency referred to the tRNA aminoacylation efficiency of *Eco*DRS for *Eco* $tRNA^{Asp}$ [$L = (k_{cat}/K_M)_{Eco\ system}/(k_{cat}/K_M)_{other}$]; b$\Delta\Delta G$ is the variation of the free energy change at the transition state when comparing aminoacylation in the homologous *Eco* system with the reactions in the heterologous or *Hsa* mt-systems [$\Delta\Delta G = -RT\ lnL$] (37); nd for not detectable.

Table 2. Crystallographic analysis of *Hsa*DRS2

Data collection statistics	
Beamline	SLS/X10A
Space group (number)	*P*2 (3)
Unit cell lengths a, b, c (Å)	142.4, 82.6, 146.3
Unit cell angles α, β, γ (°)	90, 100.4, 90
Resolution range (A)	82–3.7
Highest resolution shell (Å)	3.8–3.7
Number of observations0	255 882 (9662)
Number of unique reflections	35 768 (2403)
Completeness (%)	98.8 (91.2)
Multiplicity	7.2 (4.0)
R_{merge}/R_{meas} (%)[a]	18.0 (63.9)/19.4 (72.5)
$<I/\sigma(I)>$	9.4 (2.1)
Crystal mosaicity (°)	0.25
Asymmetric unit content	2 dimers
Solvent content (%)	62
Refined atomic structure	
Resolution range (Å)	30–3.7
R-factor/R-free (%)	22.1/28.0
Number of protein residues/atoms	4 × 589/18 840
Rmsd and bonds (Å) and angles (°)°	0.005/1.08
Ramachandran plot[b] residues in most favored unfavored regions (%)	89.2/0.2
PDBid	4AH6

Values in parentheses are for the highest resolution shell.
[a]$R_{merge} = \Sigma_{hkl}\ \Sigma_i\ |I_i(hkl) - <I(hkl)>|/\Sigma_{hkl}\ \Sigma_i\ I_i(hkl)$ and redundancy-independent; $R_{meas} = \Sigma_{hkl}\ (n/n\text{-}1)^{1/2}\ \Sigma_i\ |I_i(hkl) - <I(hkl)>|/\Sigma_{hkl}\ \Sigma_i\ I_i(hkl)$.
[b]Analysis carried out with Molprobity in Phenix package.

Altogether, 96% of the sequence of the crystallized homodimeric *Hsa*DRS2 is seen (Figure 1A), with a slight asymmetry between its two subunits because of variations in the bacterial insertion domain (Supplementary Figure S4 and Supplementary Table S5). Overall, the architecture of *Hsa*DRS2 is similar to that of bacterial DRSs, in agreement with sequence conservation (16,36). Comparison with *Eco*DRS crystal structure (30) highlighted a strong conservation. Respective DRS cores, including the anticodon-binding domain, which adopts the so-called OB fold (for oligonucleotide-binding fold), the hinge region and the catalytic domain with its characteristic antiparallel β-sheet (30,38) displayed an overall rmsd (root mean square distance) of ∼2 Å (Supplementary Table S5). These three domains shared a similar position with respect to the dimer interface. The main difference between the two aaRSs resulted from the bacterial insertion that underwent a rigid-body counterclockwise rotation of ∼26° and clearly made the mitochondrial active site more open for the binding of tRNA (Figure 1B and C). The overall fold of the insertion remained unchanged. This reorientation explains why the insertion was barely visible on the initial maps. Minor conformational diversity occurred in protein segments that diverge in sequence, located in the periphery of the catalytic domain, the flipping loop and the motif 2 loop (short insertions/deletions, see Supplementary Figure S1), which are extremely mobile in DRSs (39,40).

Based on the structural knowledge on human mt-$tRNA^{Asp}$ (41) a model of the complex with *Hsa*DRS2 could be built (Figure 2) and allowed for comparison with the bacterial complex. Notable alterations in the charge distribution within the tRNA interaction surface of the proteins were observed. Electropositive patches render *Hsa*DRS2 more attractive for its RNA partner (Figure 2), similar to what was observed in the three other mt-aaRS crystal structures solved so far (18–21) (Figure 5). Ten additional basic residues (nine Lys and an Arg highlighted in blue in Supplementary Figure S1) are inserted in the close neighborhood of *Hsa*DRS2 catalytic cleft. They may contribute to make the surface more attractive or directly contact the tRNA backbone, especially in the hinge region where such kind of aspecific interactions with the D-stem was described in the *E. coli* complex (30). Otherwise, almost all residues making direct and specific interactions with bases at both ends of the *Eco* tRNA are conserved in the human enzyme (indicated in green in Supplementary Figure S1). This is true for E270/R271/R274 or R599, which may contact C74 or nucleotides 69–70, respectively, as well as for Q129/E140, R75/Q91/R125, R125, which are adequately positioned to interact with the anticodon bases C34, U35 and G36, respectively. A few residues (indicated in orange in Supplementary Figure S1) differ without major implication for the conservation of the interaction network. Thus, the main modification is the presence of a Gly at position 269, instead of the usually conserved Asp, which accounts for the insensitivity of *Hsa*DRS2 to the nature of the discriminator base 73 (42).

The dimeric interfaces of both DRSs differ notably by the distribution and nature of subunit/subunit contacts (Supplementary Figure S6). In total, 70 hydrogen bonds

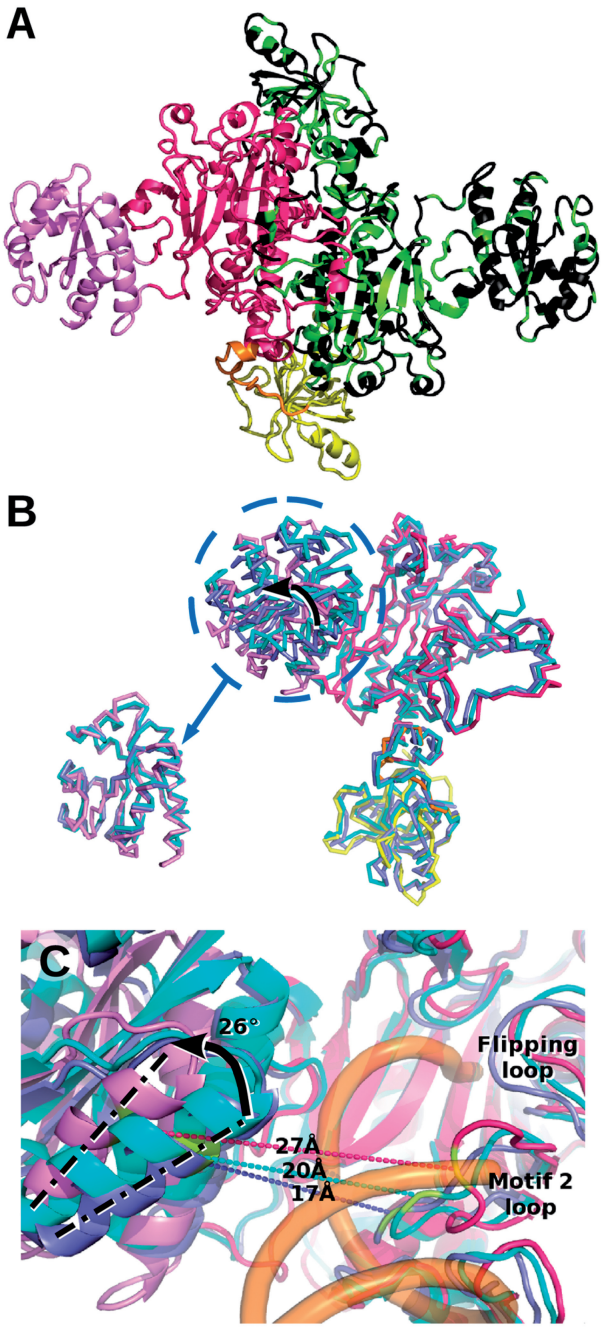

Figure 1. Newly solved 3D structure of *Hsa*DRS2 in comparison with *Eco*DRS. (**A**) Cartoon representation of *Hsa*DRS2 dimer. Characteristic DRS domains are highlighted in the left monomer: anticodon binding domain in yellow, hinge region in orange, catalytic domain in red and bacterial insertion in violet. The right monomer is displayed in black with position of residues conserved in *Hsa*DRS2, and *Eco*DRS is colored in green. Sequence identity is 40% overall, 47% in the catalytic domain, 41% for the anticodon-binding domain and drops to 25% in the insertion. (**B**) Superposition of DRS monomers: *Hsa*DRS2 chain colored as in (A), *E. coli* free (PDBid: 1EQR) and tRNA-bound (PDBid: 1C0A) monomers in light and dark blue, respectively. The bacterial insertion in *Hsa*DRS2 is rotated by 26° compared with its position in *Eco*DRS (see arrow). Bottom left: zoom on superposed insertions illustrating the overall fold conservation. (**C**) Zoom on the active site groove with same color code for DRSs as in (B), and *Eco* tRNA is represented as a semi-transparent orange backbone. The distance between two conserved residues (in green) on each side of the groove is displayed: Phe390 in *Hsa*DRS2 (Phe340 in *Eco*DRS) in the external helix of the insertion and Arg271 (Arg222) in the motif 2 loop of class II synthetases. The 26° reorientation visualized by the movement of the axis of the external helix opens up the groove for the tRNA acceptor arm by 7–10 Å in *Hsa*DRS2 when compared with the tRNA bound and free states of *Eco*DRS.

and 28 salt bridges stabilize the *Eco*DRS interface, whereas *Hsa*DRS2 only contains 60 hydrogen bonds and 20 salt bridges. Considering a 10% larger interface area (5500 versus 5100 Å^2), the contribution of specific interactions is 25% lower per Å^2, whereas the contribution of aspecific van der Waals interactions is increased, which may on average lead to a less cohesive *Hsa*DRS2 dimer.

Altogether, the crystal structure of *Hsa*DRS2 reveals that it shares the same global architecture with *Eco*DRS but differs by an enlarged catalytic groove, by a more electropositive surface potential and by a modified network of interactions in the dimer interface.

Temperature stability of *Hsa*DRS2 versus *Eco*DRS

The sensitivity of both proteins to temperature has been compared using DLS and differential scanning fluorimetry (Figure 3 and Supplementary Figure S7). *Hsa*DRS2 unfolded at a temperature of >12°C below that of *Eco*DRS, in the 37°C–45°C range, under various biochemical conditions and in the presence of various additives. This result is supported by sets of synchrotron radiation circular dichroism spectra recorded at temperatures from 20°C to 80°C (Supplementary Figure S8). For both proteins, a transition from an ordered to a disordered state occurs at temperatures similar to those observed in DLS and differential scanning fluorimetry. This low melting temperature was also valid for an *Hsa*DRS2 variant bearing different N- and C-terminal amino acids but not for *Hsa*YRS2, which melted at ~55°C (Supplementary Figure S7). Significant stabilization was observed in the presence of Asp–AMS [(5′-O-[N-(L-aspartyl)sulfamoyl]adenosine; Glu-AMS, Gln-AMS, Tyr-AMS for other sulfamoyl-adenylates; AspOH, GluOH, TyrOH for amino alcohol-adenylates], a high affinity analog of the aspartylation reaction transition state (43), but neither in the presence of tRNA, adenosine triphosphate or aspartic acid did (Figure 3 and Supplementary Figure S7). Asp–AMS had a specific effect at a 1:1 stoichiometry per monomer (not shown), suggesting that it is binding to the catalytic site and that this binding protects the protein from melting. Stabilization of aaRSs by binding of adenylate analogs has been taken advantage for successful crystallization (44). Herein, we observe stabilization against temperature induced melting. Along initial attempts to stabilize *Hsa*DRS2 by site-directed mutagenesis, the replacement of amino acids of the hinge domain by those of *Eco*DRS led to a gain of 5°C in Tm (Supplementary Figure S7).

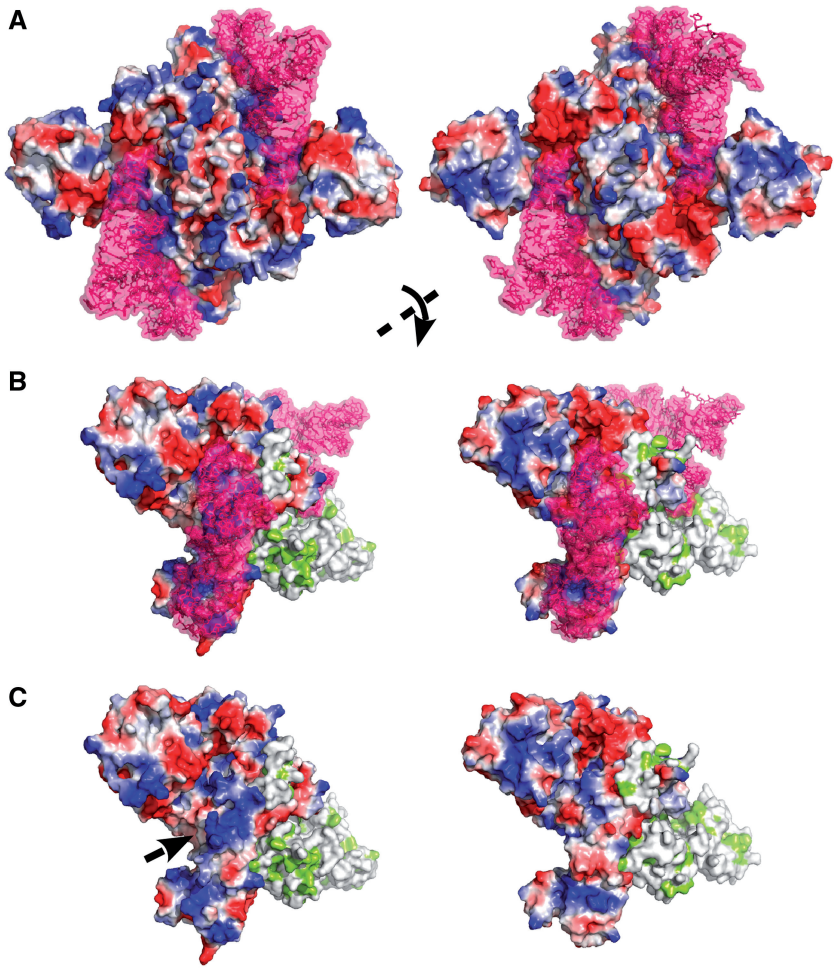

Figure 2. Comparison of *Hsa*DRS2 (left) and *Eco*DRS (right) surface potentials. Surface potentials are depicted from positive to negative in blue to red with the same color scale. (**A** and **B**), tRNA-bound *Hsa*DRS2 (model) and *Eco*DRS (PDBid: 1C0A) with $tRNA^{Asp}$ (shown in purple). (**C**) The enzymes without tRNA. In (A), the complexes are observed along their two-fold symmetry axis. In (B and C), they are rotated as indicated to better visualize the interaction zone on the surface of the left monomer. The right monomer is colored with hydrophobic patches in green.

Thermodynamics of tRNA binding to *Hsa*DRS2 versus *Eco*DRS

ITC (45) was used to gain insights into the thermodynamics of $tRNA^{Asp}$ binding to DRSs. *In vitro* transcribed tRNAs were used, as access to milligram amounts of native human mt-tRNAs remains out of scope (9). Mt-$tRNA^{Asp}$ distinguishes drastically from bacterial $tRNA^{Asp}$ by primary, secondary and tertiary structural elements (Supplementary Figure S1), leading to the absence of major aspartate identity elements and to a larger structural flexibility (25). Typical thermodynamic data are presented in Figure 4 and summarized in Table 3. Under the tested conditions, the affinities of *Hsa*DRS2 for either mt- or *Eco* $tRNA^{Asp}$ were in the same range (K_d ~250 nM), whereas binding of *Eco*DRS to its cognate $tRNA^{Asp}$ was weaker by one order of magnitude (K_d of 3 μM) and binding to the non-cognate mt-$tRNA^{Asp}$ dropped the affinity by two orders of magnitude (K_d of 22 μM). Enthalpy and entropy contributions distinguished mitochondrial and bacterial cognate complex formation. *Hsa*DRS2/mt-$tRNA^{Asp}$ was accompanied by about twice as large contributions of both parameters than *Eco*DRS/*Eco* $tRNA^{Asp}$ formation. However, both values compensated each other to similar extents, leading to similar variations in free energy namely $\Delta G = -9.1$ kcal/mol and -7.5 kcal/mol, respectively. The difference between these free energies ($\Delta\Delta G = -1.6$ kcal/mol) is in agreement with a $\Delta\Delta G$ of -2.45 kcal mol^{-1} measured by comparative kinetic properties of both aaRSs at the transition state (Table 1, 3, and 4).

Thermodynamic parameters for non-cognate complex formation (cross-complexes) revealed a pre-eminent role of the tRNA partner as compared with the synthetases (Table 4 and Figure 4A and B). Similarly, low binding enthalpies and entropies drive complexes involving the structurally stable *Eco* $tRNA^{Asp}$ regardless the enzyme. At opposite, binding of the unstable and highly flexible mt-$tRNA^{Asp}$ required far larger enthalpic and entropic compensations, regardless the enzyme. These large values are indicative of the adaptation of mt-$tRNA^{Asp}$ to both enzymes' surfaces involving likely conformational changes of the tRNA, releasing of water molecules along the binding surface and reciprocal adaptation of the nucleic acid and the protein.

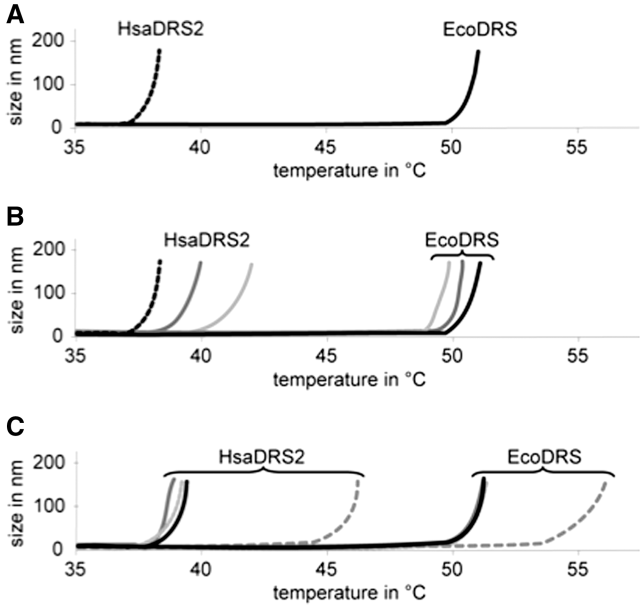

Figure 3. Thermostability of *Hsa*DRS2 and *Eco*DRS. Melting temperatures as measured by DLS. (**A**) Thermostability of *Hsa*DRS2 (dashed black line) compared with *Eco*DRS (black line). (**B**) The presence of *in vitro* transcribed *Hsa* mt-tRNA^{Asp} (light grey) or *Eco* tRNA^{Asp} (dark grey) (in 1.2-fold molar excess) did not significantly influence the thermostability of either DRS. (**C**) Among the small substrates, only Asp–AMS (dashed grey line) influences the thermostability of the two enzymes positively [aspartic acid: black line, adenosine triphosphate (ATP): grey line, AspOH: light grey line]. Denaturation temperatures of duplicates performed with different enzyme preparations differed by ≤2°C.

Thermodynamics of adenylate analog binding to *Hsa*DRS2 versus *Eco*DRS

Binding of the adenylate analog Asp–AMS to the two dimeric DRSs revealed two different binding sites within each DRS dimer (Figure 4 and Table 4). For both enzymes, a first adenylate bound to one monomer (n ∼0.5, i.e. 0.5 mol of adenylate per mol of monomer) with low affinity (Kd of 129 nM for *Hsa*DRS2 and 29.5 nM for *Eco*DRS). The second adenylate bound then to the second site with a higher affinity (Kd of 17.5 nM for *Hsa*DRS2 and of 2.95 nM for *Eco*DRS), in favor of a positive-allosteric event. The gain in affinity for the second binding site was of similar amplitude (5- to 10-fold) in both enzymes, and affinities (in the nM range) were in agreement with the previously measured K_i values for *Hsa*DRS2 (43). Binding of Asp–AMS to each monomer, however, followed a different thermodynamic route depending on the considered enzyme. For *Eco*DRS, binding was both enthalpy- and entropy-driven. In contrast, binding to *Hsa*DRS2 was strongly enthalpy-driven. This different thermodynamic signature supports different binding mechanisms of Asp–AMS to *Hsa*DRS2 and to *Eco*DRS.

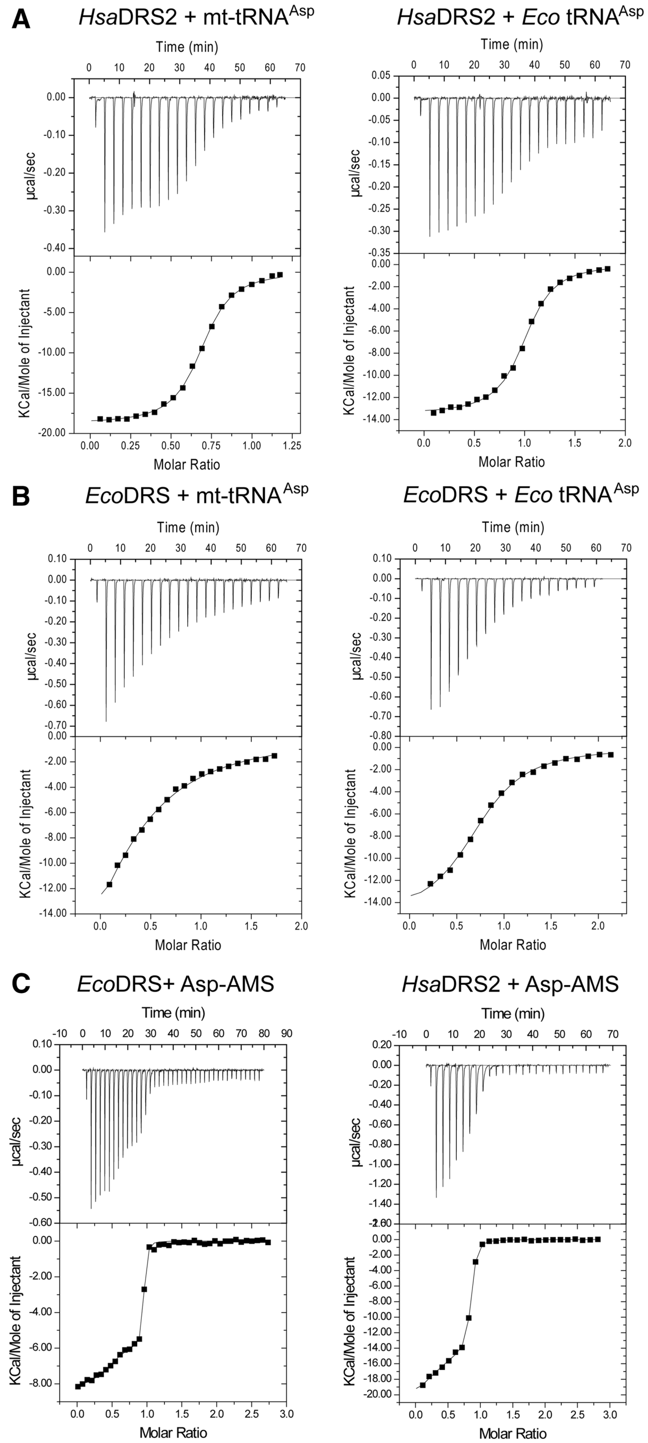

Figure 4. Isothermal titration calorimetry of *Hsa*DRS2 and EcoDRS to tRNAs and to the adenyate analog Asp–AMS. (**A**) Titration of *in vitro* transcribed tRNAs by *Hsa*DRS2. (**B**) Titration of *in vitro* transcribed tRNAs by *Eco*DRS. (**C**) Titration of *Eco*DRS and *Hsa*DRS2 by Asp–AMS.

DISCUSSION

‘Same–same but different’

The crystal structure of *Hsa*DRS2 revealed a typical overall bacterial-type DRS architecture (30, 38–40) that superimposes with the structure of *Eco*DRS with a global rmsd <2 Å (Figure 1). The two functionally important domains, catalytic site and anticodon-binding domain overlap with an rmsd of <1.5 Å. The important differences between the two structures are (i) the angle formed by the

Table 3. Comparative thermodynamic properties of *Hsa*DRS2 and *Eco*DRS: thermodynamic parameters of DRS interaction with tRNA, as measured by ITC

DRS + tRNA(transcripts)	n[a]	K_d (μM)	ΔH (kcal mol^{-1})	−TΔS (kcal mol^{-1})	ΔG (kcal mol^{-1})
*Hsa*DRS2 + *Hsa* mt-tRNA^{Asp}	0.48 ± 0.26	0.26 ± 0.18	−20.3 ± 0.7	+11.2 ± 0.4	−9.1 ± 0.5
*Hsa*DRS2 + *Eco* tRNA^{Asp}	0.87 ± 0.16	0.24 ± 0.01	−14.0 ± 0.7	+5.0 ± 0.7	−9.0 ± 0.5
*Eco*DRS + *Eco* tRNA^{Asp}	0.76 ± 0.01	3.1 ± 0.1	−13.0 ± 3.1	+5.5 ± 3.2	−7.5 ± 0.5
*Eco*DRS + *Hsa* mt-tRNA^{Aspb}	0.39 ± 0.02	22.0	−30.8	+24.4	−6.4

All data were obtained at 25°C (T = 298°K) and correspond to mean values from at least duplicated experiments with independent and freshly prepared enzyme and tRNA lots.
[a]n stands for the number of moles of Asp–AMS bound per mole of DRS monomer.
[b]Cross-binding between *Eco*DRS and *Hsa* mt-tRNA^{Asp} performed only once.

Table 4. Comparative thermodynamic properties of *Hsa*DRS2 and *Eco*DRS: thermodynamic parameters of DRS interaction with Asp–AMS, as measured by ITC

DRS + Asp-AMS	n[a]	K_d (nM)	ΔH (kcal mol^{-1})	−TΔS (kcal Mol^{-1})	ΔG (kcal mol^{-1})
*Hsa*DRS2–monomer 1	0.48 ± 0.02	129 ± 38.0	−13.18 ± 0.39	+3.9 ± 0.78	−9.38 ± 0.18
*Hsa*DRS2–monomer 2	0.29 ± 0.04	17.5 ± 12.0	−21.8 ± 0.31	+10.57 ± 0.71	−10.63 ± 0.44
*Eco*DRS–monomer 1	0.49 ± 0.02	29.5 ± 5.0	−5.50 ± 0.01	−4.75 ± 0.13	−10.24 ± 0.10
EcoDRS–monomer 2	0.44 ± 0.01	2.95 ± 1.34	−8.16 ± 0.35	−3.52 ± 0.61	−11.63 ± 0.28

All data were obtained at 25°C (T = 298°K) and correspond to mean values from at least duplicated experiments with independent and freshly prepared enzyme and tRNA lots.
[a]n stands for the number of moles of Asp–AMS bound per mole of DRS monomer.

prokaryal-specific insertion domain and the catalytic domain, which is more opened by 26° in the mt-aaRS; (ii) the overall electropositive surface potential (as observed for other mammalian mt-aaRSs); and (iii) the dimer interface, which is weaker in terms of salt-bridges and hydrogen bonds.

A distinguishing property between the two proteins is the unprecedented observation for a human mt-aaRS to melt at near body temperature (37°C) and ~12°C lower than *Eco*DRS, in line with a restricted thermo-tolerance of the translation and replication processes in mitochondria (46). It is likely that the weakened dimer interface is one of the contributors to this fragility. Fine prediction of the molecular reasons for the melting temperature of a protein is difficult and may be dependent on as little as a single amino acid (47). Interestingly, a thermosensitive mutant of *Eco*DRS in which proline 555 was affected, has been reported (48). The equivalent position in *Hsa*DRS2 has kept an equivalent proline residue (Pro 605), so that the contribution of this position to thermosensitivity is ruled out. We favor the contribution of the hinge domain, as partial stabilization by mutation in *Hsa*DRS2 was successful.

ITC was used here for the first time on tRNA/synthetase couples to examine thermodynamics of cognate mt-tRNA^{Asp} and non-cognate *Eco* tRNA^{Asp} interactions. When tested under strictly the same conditions, *Hsa*DRS2 binds both its cognate and non-cognate tRNA^{Asp} with a same sub-micromolar Kd, whereas *Eco*DRS binds cognate *Eco* tRNA^{Asp} in the low micromolar range and non-cognate mt-tRNA^{Asp} in the high micromolar range. It is anticipated that the parameters would be closer to, but still distinct, from those for the bacterial cognate pair when measured with native post-transcriptionally modified tRNAs. Indeed, modifications are known to stabilize structures (49), but the modification pattern of mt-tRNA^{Asp} is far beneath that of *Eco* tRNA^{Asp} (see Supplementary Figure S1). Binding between cognate mitochondrial partners requires large enthalpic and entropic compensations at opposite to binding between the cognate bacterial partners where compensations were small. Cross-binding revealed that this difference is mostly linked to the tRNA. Binding of the floppy mt-tRNA involved large positive enthalpic and large negative entropic contributions, whereas binding of the well-folded and stable *Eco* tRNA involved low enthalpy/entropy compensations. These results are in line with thermodynamic parameters determined for cognate and non-congate tRNA/synthetase couples measured earlier by fluorescence titrations and fast kinetic techniques (50,51).

Altogether, comparative investigation of biophysical properties of *Hsa*DRS2 and *Eco*DRS shed new light on the long-term open question as to non-reciprocal aminoacylation of bacterial and mitochondrial tRNA/synthetase pairs (24). They revealed that the human enzyme has gained structural adaptability to tRNA substrates by combining several properties. A more electropositive tRNA-binding surface [see also (52)] and an opening of the cleft between the insertion domain and the catalytic domain by an angle of as much as 26° improve accessibility and binding of the tRNA end to the catalytic site. Strong binding likely reflects an evolutionary adaptation of the mt-aaRS to compensate for high flexibility of the mt-tRNA and for the absence of otherwise important identity elements. Whether the

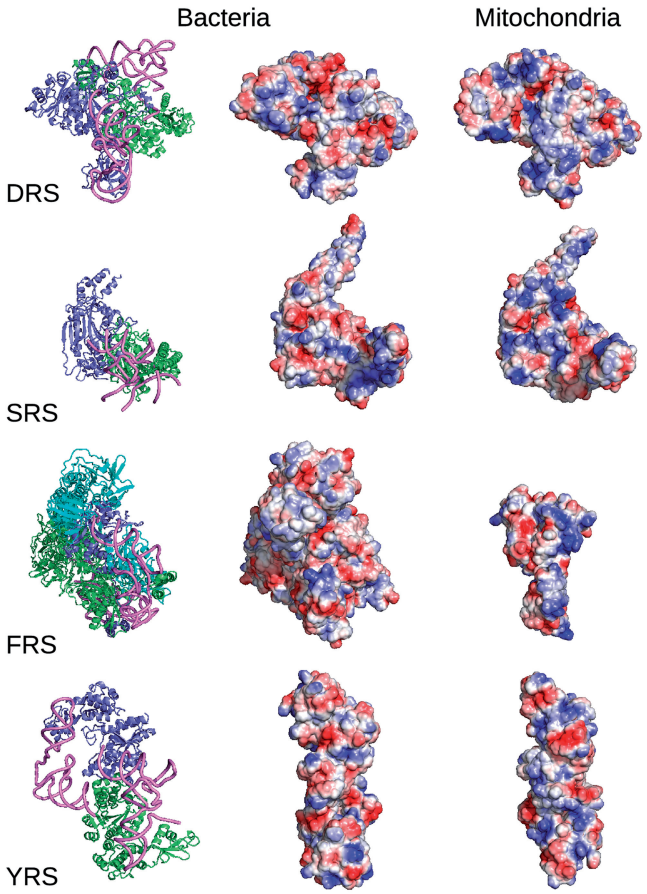

Figure 5. Molecular surface potential of bacterial (*E. coli* or *Thermus thermophilus*) and mammalian (bovine or human) mitochondrial aaRSs. On the left, bacterial complexes (PDBids: 1C0A for *Eco*DRS/tRNA, 1SRS for *Tth*SRS/tRNA, 2IY5 for *Tth*FRS/tRNA and 1H3E for *Tth*YRS/tRNA) are shown on the left with monomers A in blue, monomers B in green and tRNAs in pink, indicating the binding site of the cognate substrates. In the case of tetrameric bacterial FRS, monomers C and D are depicted in cyan. The electrostatic surface potential of free aaRS forms is represented in the same orientation as the complexes for bacterial (1EQR for *Eco*DRS, 1SRY for *Tth*SRS, 1B7Y for *Tth*FRS, 1H3F for *Tth*YRS without its C-terminal domain) and mitochondrial enzymes (this study for *Hsa*DRS2, 1WLE for *Bta*SRS2, 3TUP for *Hsa*FRS2, 2PID for *Hsa*YRS2). Overall, the tRNA binding surface seems to be more electropositive in mitochondrial forms, even for FRS, which has a different structural organization (monomer instead of heterotetramer).

binding step is accompanied by a concerted movement of the insertion domain towards the catalytic site to further lock the tRNA, is unknown. The larger structural plasticity of the mt-aaRS (enabling it to deal with the highly flexible and degenerated mt-tRNA^{Asp}) does not harm its interaction with classical and less flexible *Eco* tRNA^{Asp}. At opposite, the bacterial aaRS is unable to bind properly the mt-tRNA. Binding to its cognate more rigid tRNA^{Asp} is closer to a lock-and-key type process.

Gain of plasticity as reflected here by unusual thermodynamic properties, may be a more general property of mt-aaRSs that have to deal with degenerated mt-tRNAs. An extreme case of plasticity has recently been described with the human mitochondrial FRS that undergoes dramatic conformation change on tRNA binding (21). The near-body thermal unstability of *Hsa*DRS2 as well as its electropositive surface potential suggest that different parameters may stabilize the protein *in vivo*. These may be of biochemical nature or correspond to co-factors, partner proteins or peculiar sub-mitochondrial localization, as is the case for mt-ribosomes and mt-elongation factor that bind to the inner membrane (9).

Cooperative allostery in class II dimeric DRSs

A long-standing question for dimeric aaRSs concerns the communication mechanisms between the two catalytic sites (13). Data obtained herein by ITC demonstrate unambiguously that both *Eco*DRS and *Hsa*DRS2 undergo an allosteric event on binding to the adenylate analog. The first monomer binds the analog with a weaker affinity than the second monomer. Thermodynamic signatures strongly suggest a different binding mechanism for each enzyme: interaction with *Hsa*DRS2 is a strongly exothermic process, characterized by a large negative enthalpic term, whereas binding to *Eco*DRS is associated with moderate enthalpic and entropic contributions. These differences likely reflect large obligatory rearrangements in *Hsa*DRS2 but not in *Eco*DRS.

Allostery has been reported for several aaRSs (53–56). Half of the site activity was mainly observed. Herein, we report direct cooperative allostery for small substrate binding, as detected by ITC. Previous ITC investigations performed on other aaRSs had not detected cooperative allostery (53–56).

CONCLUSION AND PERSPECTIVES

Resolution of the crystal structure and exploration of biophysical properties of a human mitochondrial aaRS, revealed similarities but also distinctive features from a prokaryotic homolog: a conserved architecture and a conserved cooperative allosteric communication within the dimers but also increased structural plasticity. We propose that the modification of intrinsic biophysical properties and new surface properties, along with conservation of size and structural framework, represents an evolutionary mechanism for adaptation of nuclear-encoded proteins to degenerated mitochondrial-encoded RNAs. This mechanism is alternative to domain extension and sustains adaptation of two genomes subjected to different evolutionary constraints. The possibility that mt-aaRSs also undergo functional expansion by structural inventions and have partner proteins as described for cytosolic aaRSs (57,58) is not excluded but remains to be tackled. The properties of an mt-aaRS reported herein provide new insights towards the understanding of the growing number of human disorders linked to mutations in the corresponding genes (9,59,60). Deciphering the fine molecular triggers leading to both specific (i.e. plasticity) and shared (i.e. allostery) properties of human mt-aaRSs, and their evolutionary related homologs requires delineation of discriminating and non-discriminating amino acids within the aaRS

architecture. Bioinformatic tools enabling such an analysis are under development.

ACCESSION NUMBERS

The coordinates and structure factors are deposited in the Protein Data Bank under the accession code 4AH6.

SUPPLEMENTARY DATA

Supplementary Data are available at NAR Online: Supplementary Figures 1–4 and 6–8, Supplementary Table 5 and Supplementary References [61–63].

ACKNOWLEDGEMENTS

The authors thank R. Giegé and P. Dumas for fruitful discussions, G. Eriani for gift of material, R. David and the team of the high-performance computing facility for allocating CPU time to the project to carry out extensive DEN refinement on HsaDRS2 structure (HPC méso-centre de calcul, Université de Strasbourg), V. Olieric and the PX team at the Swiss Light Source (Villigen, Switzerland), as well as Frank Wien and the staff of DISCO at SOLEIL synchrotron (Saint-Aubin, France) for beamtime allocation and assistance during data collection.

FUNDING

Association Française contre les Myopathies (AFM); Agence Nationale pour la Recherche [ANR-09-BLAN-0091-01/03, ANR-PCV07-187047]; French National Program 'Investissements d'Avenir' (Labex MitoCross); Centre National de la Recherche Scientifique (CNRS); Université de Strasbourg; France Diplomatie [200930]. Funding for open access charge: Centre National pour la Recherche Scientifique (CNRS).

Conflict of interest statement. None declared.

REFERENCES

1. Gray,M.W., Burger,G. and Lang,B.F. (1999) Mitochondrial evolution. *Science*, **283**, 1476–1481.
2. Anderson,S., Bankier,A.T., Barrel,B.G., de Bruijn,M.H.L., Coulson,A.R., Drouin,J., Eperon,J.C., Nierlich,D.P., Roe,B.A., Sanger,F. *et al*. (1981) Sequence and organization of the human mitochondrial genome. *Nature*, **290**, 457–465.
3. Brown,W.M., George,M. and Wilson,A.C. (1979) Rapid evolution of animal mitochondrial DNA. *Proc. Natl Acad. Sci. USA*, **76**, 1967–1971.
4. Castellana,S., Vicario,S. and Saccone,C. (2011) Evolutionary patterns of the mitochondrial genome in Metazoa: exploring the role of mutation and selection in mitochondrial protein coding genes. *Genome Biol. Evol.*, **3**, 1067–1079.
5. Smits,P., Smeitink,J. and van den Heuvel,L. (2010) Mitochondrial translation and beyond: processes implicated in combined oxidative phosphorylation deficiencies. *J. Biomed. Biotechnol.*, **2010**, 1–24.
6. Watanabe,K. (2010) Unique features of animal mitochondrial translation systems. The non-universal genetic code, unusual features of the translational apparatus and their relevance to human mitochondrial diseases. *Proc. Jpn. Acad. Ser. B Phys. Biol. Sci.*, **86**, 11–36.
7. Holzmann,J., Frank,P., Löffler,E., Bennett,K.L., Gerner,C. and Rossmanith,W. (2008) RNase P without RNA: identification and functional reconstitution of the human mitochondrial tRNA processing enzyme. *Cell*, **135**, 462–474.
8. Helm,M., Brulé,H., Friede,D., Giegé,R., Pütz,J. and Florentz,C. (2000) Search for characteristic structural features of mammalian mitochondrial tRNAs. *RNA*, **6**, 1356–1379.
9. Suzuki,T., Nagao,A. and Suzuki,T. (2011) Human mitochondrial tRNAs: biogenesis, function, structural aspects, and diseases. *Annu. Rev. Genet.*, **45**, 299–329.
10. Giegé,R., Jühling,F., Pütz,J., Stadler,P., Sauter,C. and Florentz,C. (2012) Structure of transfer RNAs: similarity and variability. *Wiley Interdiscip. Rev. RNA*, **3**, 37–61.
11. Sharma,M.R., Koc,E.C., Datta,P.P., Booth,T.M., Spremulli,L.L. and Agrawal,R.K. (2003) Structure of the mammalian mitochondrial ribosome reveals an expanded functional role for its component proteins. *Cell*, **115**, 97–108.
12. Smits,P., Smeitink,J.A., van den Heuvel,L.P., Huynen,M.A. and Ettema,T.J. (2007) Reconstructing the evolution of the mitochondrial ribosomal proteome. *Nucleic Acids Res.*, **35**, 4686–4703.
13. Ibba,M., Francklyn,C. and Cusack,S. (2005) *The Aminoacyl-tRNA Synthetases*. Landes Biosciences, Georgetown, TX.
14. Woese,C.R., Olsen,G.J., Ibba,M. and Söll,D. (2000) Aminoacyl-tRNA synthetases, the genetic code, and the evolutionary process. *Microbiol. Mol. Biol. Rev.*, **64**, 202–236.
15. Sissler,M., Pütz,J., Fasiolo,F. and Florentz,C. (2005) Mitochondrial aminoacyl-tRNA synthetases. In: Ibba,M., Francklyn,C. and Cusack,S. (eds), *Aminoacyl-tRNA Synthetases*, Landes Biosciences, Georgetown, TX, Vol. Chap 24, pp. 271–284.
16. Bonnefond,L., Fender,A., Rudinger-Thirion,J., Giegé,R., Florentz,C. and Sissler,M. (2005) Toward the full set of human mitochondrial aminoacyl-tRNA synthetases: characterization of AspRS and TyrRS. *Biochemistry*, **44**, 4805–4816.
17. Brindefalk,B., Viklund,J., Larsson,D., Thollesson,M. and Andersson,S.G. (2007) Origin and evolution of the mitochondrial aminoacyl-tRNA synthetases. *Mol. Biol. Evol.*, **24**, 743–756.
18. Chimnaronk,S., Gravers Jeppesen,M., Suzuki,T., Nyborg,J. and Watanabe,K. (2005) Dual-mode recognition of noncanonical tRNAs(Ser) by seryl-tRNA synthetase in mammalian mitochondria. *EMBO J.*, **24**, 3369–3379.
19. Bonnefond,L., Frugier,M., Touzé,E., Lorber,B., Florentz,C., Giegé,R., Sauter,C. and Rudinger-Thirion,J. (2007) Crystal structure of human mitochondrial tyrosyl-tRNA synthetase reveals common and idiosyncratic features. *Structure*, **15**, 1505–1516.
20. Klipcan,L., Levin,I., Kessler,N., Moor,N., Finarov,I. and Safro,M. (2008) The tRNA-induced conformational activation of human mitochondrial phenylalanyl-tRNA synthetase. *Structure*, **16**, 1095–1104.
21. Klipcan,L., Moor,N., Finarov,I., Kessler,N., Sukhanova,M. and Safro,M.G. (2012) Crystal structure of human mitochondrial PheRS complexed with tRNA(Phe) in the active "open" state. *J. Mol. Biol.*, **415**, 527–537.
22. Florentz,C., Sohm,B., Tryoen-Tóth,P., Pütz,J. and Sissler,M. (2003) Human mitochondrial tRNAs in health and disease. *Cell. Mol. Life Sci.*, **60**, 1356–1375.
23. Bonnefond,L., Frugier,M., Giegé,R. and Rudinger-Thirion,J. (2005) Human mitochondrial TyrRS disobeys the tyrosine idenity rules. *RNA*, **11**, 558–562.
24. Kumazawa,Y., Himeno,H., Miura,K.-I. and Watanabe,K. (1991) Unilateral aminoacylation specificity between bovine mitochondria and eubacteria. *J. Biochem.*, **109**, 421–427.
25. Fender,A., Gaudry,A., Jühling,F., Sissler,M. and Florentz,C. (2012) Adaptation of aminoacylation rules to mammalian mitochondria. *Biochimie*, **94**, 1090–1097.
26. Gaudry,A., Lorber,B., Messmer,M., Neuenfeldt,A., Sauter,C., Florentz,C. and Sissler,M. (2012) Redesigned N-terminus enhances expression, solubility, and crystallisability of mitochondrial enzyme. *Protein Eng. Des. Sel.*, **25**, 473–481.
27. Sissler,M., Lorber,B., Messmer,M., Schaller,A., Pütz,J. and Florentz,C. (2008) Handling mammalian mitochondrial tRNAs and aminoacyl-tRNA synthetases for functional and structural characterization. *Methods*, **44**, 176–189.

28. Kabsch,W. (2010) Integration, scaling, space-group assignment and post-refinement. *Acta Crystallogr. D Biol. Crystallogr.*, **66**, 133–144.
29. Collaborative Computational Project,N. (1994) The CCP4 suite: programs for protein crystallography. *Acta Crystallogr. D Biol. Crystallogr.*, **50**, 760–763.
30. Eiler,S., Dock-Bregeon,A.C., Moulinier,L., Thierry,J.-C. and Moras,D. (1999) Synthesis of aspartyl-tRNA^{Asp} in *Escherichia coli*-a snapshot of the second step. *EMBO J.*, **18**, 6532–6541.
31. McCoy,A.J., Grosse-Kunstleve,R.W., Adams,P.D., Winn,M.D., Storoni,L.C. and Read,R.J. (2007) Phaser crystallographic software. *J. Appl. Crystallogr.*, **40**, 658–674.
32. Adams,P.D., Afonine,P.V., Bunkóczi,G., Chen,V.B., Davis,I.W., Echols,N., Headd,J.J., Hung,L.W., Kapral,G., Grosse-Kunstleve,R.W. *et al.* (2010) PHENIX: a comprehensive Python-based system for macromolecular structure solution. *Acta Crystallogr. D Biol. Crystallogr.*, **66**, 213–221.
33. Schröder,G.F., Levitt,M. and Brunger,A.T. (2010) Super-resolution biomolecular crystallography with low-resolution data. *Nature*, **464**, 1218–1222.
34. Cummings,M.D., Farnum,M.A. and Nelen,M.I. (2006) Universal Screening Methods and Applications of ThermoFluor®. *J. Biomol. Screen.*, **11**, 854–863.
35. Lees,J.G., Smith,B.R., Wien,F., Miles,A.J. and Wallace,B.A. (2004) CDtool-an integrated software package for circular dichroism spectroscopic data processing, analysis, and archiving. *Anal. Biochem.*, **332**, 285–289.
36. Giegé,R. and Rees,B. (2005) Aspartyl-tRNA synthetases. In: Ibba,M., Francklyn,C. and Cusack,S. (eds), *Aminoacyl-tRNA Synthetases*, Landes Bioscience, Georgetown, TX, Vol. Chap 19, pp. 210–226.
37. Pütz,J., Puglisi,J.D., Florentz,C. and Giegé,R. (1993) Additive, cooperative and anti-cooperative effects between identity nucleotides of a tRNA. *EMBO J.*, **12**, 2949–2957.
38. Delarue,M., Poterszman,A., Nikonov,S., Garber,M., Moras,D. and Thierry,J.-C. (1994) Crystal structure of a prokaryotic aspartyl-tRNA synthetase. *EMBO J.*, **13**, 3219–3229.
39. Schmitt,E., Moulinier,L., Fujiwara,S., Imanaka,T., Thierry,J.-C. and Moras,D. (1998) Crystal structure of aspartyl-tRNA synthetase from *Pyrococcus kodakaraensis* KOD: archeon specificity and catalytic mechanism of adenylate formation. *EMBO J.*, **17**, 5227–5237.
40. Moulinier,L., Eiler,S., Eriani,G., Gangloff,J., Thierry,J.-C., Gabriel,K., McClain,W.H. and Moras,D. (2001) The structure of an AspRS-tRNA^{Asp} complex reveals a tRNA-dependant control mechanism. *EMBO J.*, **20**, 5290–5301.
41. Messmer,M., Pütz,J., Suzuki,T., Suzuki,T., Sauter,C., Sissler,M. and Florentz,C. (2009) Tertiary network in mammalian mitochondrial tRNA^{Asp} revealed by solution probing and phylogeny. *Nucleic Acids Res.*, **37**, 6881–6895.
42. Fender,A., Sauter,C., Messmer,M., Pütz,J., Giegé,R., Florentz,C. and Sissler,M. (2006) Loss of a primordial identity element for a mammalian mitochondrial aminoacylation system. *J. Biol. Chem.*, **281**, 15980–15986.
43. Messmer,M., Blais,S.P., Balg,C., Chênevert,R., Grenier,L., Lagüe,P., Sauter,C., Sissler,M., Giegé,R., Lapointe,J. *et al.* (2009) Peculiar inhibition of human mitochondrial aspartyl-tRNA synthetase by adenylate analogs. *Biochimie*, **91**, 596–603.
44. Giegé,R., Touzé,E., Lorber,B., Théobald-Dietrich,A. and Sauter,C. (2008) Crystallogenesis trends of free and liganded aminoacyl-tRNA synthetases. *Cryst. Growth Des.*, **8**, 4297–4306.
45. Leavitt,S. and Freire,E. (2001) Direct measurement of protein binding energetics by isothermal titration calorimetry. *Curr. Opin. Struct. Biol.*, **11**, 560–566.
46. Germaniuk,A., Liberek,K. and Marszalek,J. (2002) A bichaperone (Hsp70-Hsp78) system restores mitochondrial DNA synthesis following thermal inactivation of Mip1p polymerase. *J. Biol. Chem.*, **277**, 27801–27808.
47. Perl,D., Mueller,U., Heinemann,U. and Schmid,F.X. (2000) Two exposed amino acid residues confer thermostability on a cold shock protein. *Nat. Struct. Biol.*, **7**, 380–383.
48. Martin,F., Sharpless,G.J., Lloyd,R.G., Eiler,S., Moras,D., Gangloff,J. and Eriani,G. (1997) Characterization of a thermosensitive *E. coli* aspartyl-tRNA synthetase mutant. *J. Bacteriol.*, **179**, 3691–3696.
49. Motorin,Y. and Helm,M. (2010) tRNA stabilization by modified nucleotides. *Biochemistry*, **49**, 4934–4944.
50. Lam,S.S.M. and Schimmel,P.R. (1975) Equilibrium measurements of cognate and noncognate interactions between aminoacyl transfer RNA synthetases and transfer RNA. *Biochemistry*, **14**, 2775–2780.
51. Krauss,G., Riesner,D. and Maass,G. (1976) Mechanism of discrimination between cognate and non-cognate tRNAs by phenylalanyl-tRNA synthetase from yeast. *Eur. J. Biochem.*, **68**, 81–93.
52. Tworowski,D., Feldman,A.V. and Safro,M.G. (2005) Electrostatic potential of aminoacyl-tRNA synthetase navigates tRNA on its pathway to the binding site. *J. Mol. Biol.*, **350**, 866–882.
53. Buddha,M.R. and Crane,B.R. (2005) Structures of tryptophanyl-tRNA synthetase II from *Deinococcus radiodurans* bound to ATP and tryptophan. Insight into subunit cooperativity and domain motions linked to catalysis. *J. Biol. Chem.*, **280**, 31965–31973.
54. Retailleau,P., Weinreb,V., Hu,M. and Carter,C.W. (2007) Crystal structure of tryptophanyl-tRNA synthetase complexed with adenosine-5' tetraphosphate: evidence for distributed use of catalytic binding energy in amino acid activation by class I aminoacyl-tRNA synthetases. *J. Mol. Biol.*, **369**, 108–128.
55. Hussain,T., Kamarthapu,V., Kruparani,S.P., Deshmukh,M.V. and Sankaranarayanan,R. (2010) Mechanistic insights into cognate substrate discrimination during proofreading in translation. *Proc. Natl Acad. Sci. USA*, **107**, 22117–22121.
56. Dignam,J.D., Guo,J., Griffith,W.P., Garbett,N.C., Holloway,A. and Mueser,T. (2011) Allosteric interaction of nucleotides and tRNA^{Ala} with *E coli* alanyl-tRNA synthetase. *Biochemistry*, **50**, 9886–9900.
57. Park,S.G., Ewalt,K.L. and Kim,S. (2005) Functional expansion of aminoacyl-tRNA synthetases and their interacting factors: new perspectives on housekeepers. *Trends Biochem. Sci.*, **30**, 569–574.
58. Guo,M., Schimmel,P. and Yang,X.-L. (2010) Functional expansion of human tRNA synthetases achieved by structural inventions. *FEBS Lett.*, **584**, 434–442.
59. Scheper,G.C., van der Klok,T., van Andel,R.J., van Berkel,C.G., Sissler,M., Smet,J., Muravina,T.I., Serkov,S.V., Uziel,G., Bugiani,M. *et al.* (2007) Mitochondrial aspartyl-tRNA synthetase deficiency causes leukoencephalopathy with brain stem and spinal cord involvement and lactate elevation. *Nat. Genet.*, **39**, 534–539.
60. Park,S.G., Schimmel,P. and Kim,S. (2008) Aminoacyl tRNA synthetases and their connections to disease. *Proc. Natl Acad. Sci. USA*, **105**, 11043–11049.
61. Fender,A., Sauter,C., Messmer,M., Pütz,J., Giegé,R., Florentz,C. and Sissler,M. (2006) Loss of a primordial identity element for a mammalian mitochondrial aminoacylation system. *J. Biol. Chem.*, **281**, 15980–15986.
62. Sekiya,T., Mori,M., Takahashi,N. and Nishimura,S. (1980) Sequence of the distal tRNA^{Asp}1 gene and the transcription termination signal in the *Escherichia coli* ribosomal RNA operon rrnF (or G). *Nucleic Acids Res.*, **8**, 3809–3827.
63. Bonnefond,L., Frugier,M., Touzé,E., Lorber,B., Forentz,C., Giegé,R., Rudinger-Thirion,J. and Sauter,C. (2007) Tyrosyl-tRNA synthetase: the first crystallization of a human mitochondrial aminoacyl-tRNA synthetase. *Acta Crystallogr. Sect. F*, **F63**, 338–341.